Journal of Radioanalytical and Nuclear Chemistry
https://doi.org/10.1007/s10967-018-6255-9

The dark shades of the Antikythera Mechanism

Aristeidis Voulgaris[1] · Christophoros Mouratidis[2] · Andreas Vossinakis[3]

Received: 19 June 2018

Abstract
In this work we analyze the dark shades which are evident on the AMRP X-ray positive Computed Tomographies and Radiographies of the Antikythera Mechanism ancient prototype. During 2000 years under the sea, the Mechanism bronze parts were totally corroded. The decreased X-ray absorption of the corroded bronze, allowed the CTs capture even in the thick large side of Fragment A. During the photometric analysis of the CTs, apart from corroded bronze, at least two other different (corroded) metal materials were detected, which were used by the ancient manufacturer during the construction of the Antikythera Mechanism. From our analysis and correlating with the mechanical evidence resulting by the use of our functional reconstruction models of the Antikythera Mechanism, we conclude that the existing design of the Antikythera Mechanism is probably the first of such a sophisticated design of the ancient manufacturer.

Keywords Metals of Antikythera Mechanism · Bronze corrosion · Atacamite X-ray absorption

Introduction

The Antikythera Mechanism was found in 1901, in a shipwreck at 50 m depth, on a gulf of Antikythera island, Greece, by Symian sponge divers. It is a unique geared machine consisting of gears, axes, engraved plates and pointers, constructed by an unknown ancient manufacturer about 120 BC. It could predict the position of the Sun in the sky, the Lunar phases, the starting date of the athletic games, Solar and Lunar eclipses, as well as the date and hour they were about to happen [1–3]. Due to its uniqueness, the Antikythera Mechanism is exclusively exhibited in a special ward under a glass showcase for safety and conservation reasons, on the *National Archaeological Museum of Athens, Greece*.

The X-ray applications help in retracting very useful information about the design, the shape and the content materials of the ancient artifacts [4]. The study inside the Mechanism via the 2D X-ray and Thulium 170 radiation began by C. Karakalos of *National Centre of Scientific Research "Demokritos" (Greece)*, in the 1970s. Karakalos took several film radiographies @160 keV [3]. The first results of radiographies of the Mechanism were published in 1974 by D.S. Price in the work *Gears from the Greeks* [3]. The X-ray study of the Mechanism was continued by M.T. Wright and A. Bromley in the 1990s by using stereographic radiography and linear motion tomography [5, 6].

In 2005, during the implementation of the *Antikythera Mechanism Research Project* (*AMRP*), a large X-ray tomograph was used for the detailed in depth visualization, of the Antikythera Mechanism corroded fragments [1, 7, 8]. A large number of the X-ray Computed Tomographies (CTs) and radiographies of the Antikythera Mechanism were obtained Fig. 1.

In the AMRP CTs, some of the Mechanism parts inside the Fragment A, display strongly different absorption than the rest corroded bronze parts, signaling different (corroded) metal/alloy materials. The characterization of the new metals was achieved by the study of their X-ray absorption in correlation to the corroded bronze absorption.

The authors, after the extended study of AMRP CTs, reconstructed two functional models of the Antikythera Mechanism, applying the new revised gearing scheme of the Mechanism [9]. These new detected metals were used

✉ Aristeidis Voulgaris
arisvoulgaris@gmail.com; a.voulgaris@thessaloniki.gr

[1] Municipality of Thessaloniki, Directorate Culture-Tourism, Thessaloníki 54625, Greece

[2] Hellenic Ministry of Education, Research and Religious Affairs, Kos 85300, Greece

[3] Thessaloniki Astronomy Club, Thessaloníki 54646, Greece

Published online: 20 October 2018

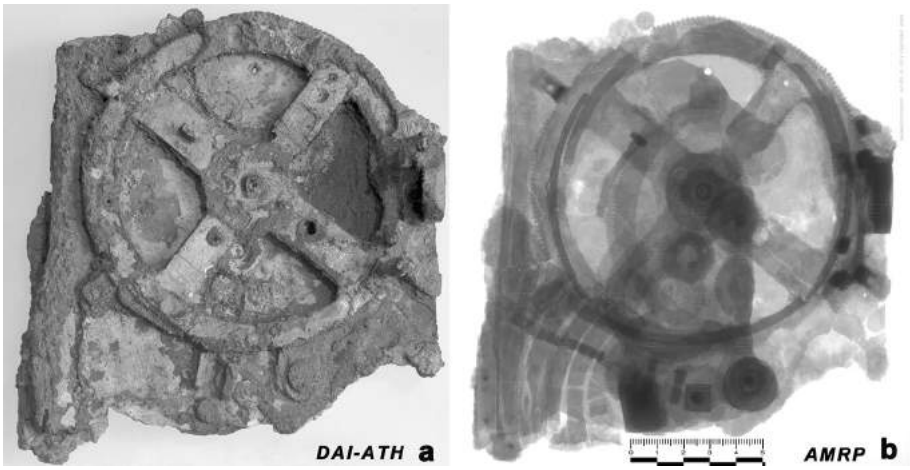

Fig. 1 **a** Visual photograph of Fragment A (probably) taken in the 1930s (Émile Seraf, © Deutsches Archäologisches Institut, D-DAI-ATH-EMILE-827), **b** same scale positive X-Ray radiography of Fragment A © AMRP. Note that the strong dark shades are caused by the total (active) thickness of the fragment, which varies because of the different distribution of the parts inside the fragment

for the construction of the corresponding mechanical parts in our functional reconstruction models and for testing during operation of the models.

According to our findings we also detected that a metal (alloy) was also used for the stabilization of some of the mechanical parts on the Middle Plate of the Mechanism [3]. Based on these observations, a discussion is also presented about the mechanical restorations/rectifies probably made by the ancient manufacturer, just after the assembly of his creation.

Theory

The X-ray absorption of the Antikythera Mechanism parts

Today the fossilized Mechanism is partially preserved in six larger fragments and 76 other smaller pieces [2, 6]. The fragments mainly have green and also beige and blue shades, as a result of the strong corrosion/chemical changes during 2000 years under the sea Fig. 2. These color shades strongly differ from the bright bronze color of the original ancient appearance.

The spectrochemical and metallurgical analysis results are described in Price 1974 [3]. The Mechanism main metal material was bronze, an alloy Cu 95% and Sn 5% ± 50%. During time under the Aegean Sea the bronze Mechanism transformed into a new material, mostly *di-copper trioxychloride* $Cu_2(OH)_3Cl$—*atacamite* (and other isomers of about equal density) and probably other—in small percentage—chemical compounds -corrosion products and impurities (which mostly have dark colors), which are not visible in the damaged area of gear *b1* arm, Fig. 2 [10–17].

Atacamite is a mineral (or corrosion product) material with lower density (3.76 g cm^{-3}) than bronze

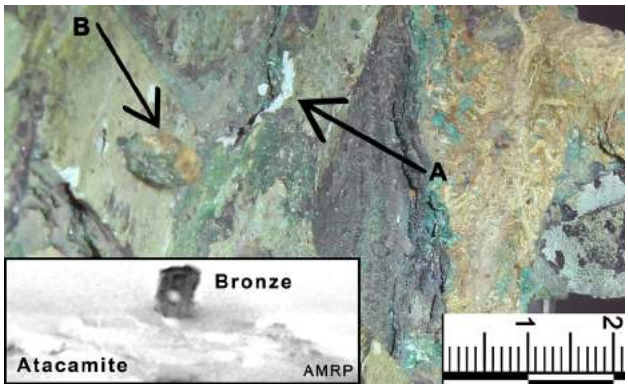

Fig. 2 Close up of the two arms of *b1* gear of Fragment A. The strong-deep inside material corrosion (atacamite) is clearly visible and the material appears homogenized, clear, without dark color chemical compounds and other impurities (arrow A). An oblong bronze colored preserved part, with non-corroded surface, of unknown operation is also visible (arrow B) *Credits*: National Archaeological Museum, Athens, A. Voulgaris, Copyright © Hellenic Ministry of Culture & Sports/Archaeological Receipts Fund. Insert image, AMRP positive CT of the bronze color oblong part. Note the strong dark shade of the bronze colored part in relation to the gray shades of the adjacent areas (atacamite) © AMRP

(8.87 g cm^{-3}). This decrease of density, because of the deep inside corrosion of the bronze material Fig. 2, made much easier the transmission of the X-rays through the corroded material, even in the relatively thick Fragment A Fig. 1. The fossilized silt material between Fragment A plates, does not significantly decrease the X-ray penetration (as it is evident in Fragment B radiography, the existing silt on the Metonic spiral gaps has much lower X-ray absorption than atacamite).

In 2005, the "*Blade Runner*", X-ray tomograph with 225 kV (up to 450 kV) micro focus X-ray source, loaned by X-Tek Systems Ltd (now owned by Nikon Metrology) was used for capturing X-ray tomographies of the Antikythera Mechanism fragments [8].

The Fragments were placed between a pinpoint-50 μm X-ray source and 40 cm × 40 cm fluorescent screen which converted the incident X-ray energy into light (fluorescence). A large number of tomographies and radiographies were captured with resolution 2000 × 2000 pixels [1, 6, 8].

The transmitted X-rays through the corroded material of the Mechanism (especially in the large Fragment A) had variable intensity because of the different local area thickness, the different absorption of the (corroded) materials, the material inhomogeneities, the presence of atmospheric air inside the gaps, the petrified silt and other impurities etc. This variable intensity was represented as projected variable bright, gray and dark shades on the fluorescent screen. The dark shade areas on positive CTs (bright on negative) correspond to the lower transmission i.e. stronger X-ray absorption of the corresponding area than the brighter adjacent areas.

Let's assume a pinpoint narrow X-ray beam of monoenergetic photons with intensity I_0, radiating into a material with thickness x and density ρ. The transmitted intensity I is given by the exponential attenuation law

$$I = I_0 e^{-\mu^* x} = I_0 e^{-(\mu^*/\rho)\rho x} = I_0 e^{-\mu\rho x} \quad (1)$$

The constant μ^* (cm^{-1}) is the linear absorption coefficient which depends on the element and $\mu = \mu^*/\rho$ ($cm^2\ g^{-1}$) is the mass absorption coefficient [18, 19]. For example, for a solid bronze piece with thickness 120 mm = 12 cm, the X-ray transmission @225 keV (the selected energy used for the X-rays, correspondence with A. Ramsey) is $I_{bronze} = 2.13 \times 10^{-7}\ I_0$ (see Table 1).

For two different materials a and b, of equal thickness x, the X-ray transmission ratio, depends only by their corresponding material characteristics i.e. density and mass absorption coefficient:

$$I_a/I_b = e^{-x(\mu_a \rho_a - \mu_b \rho_b)} \rightarrow I_a/I_b = e^{x(\mu_b^* - \mu_a^*)} \quad (2)$$

If we compare the X-ray transmission of a solid bronze material ($\mu^*_{bronze} = 1.280$, see Table 1) and a totally corroded bronze i.e. atacamite material ($\mu^*_{atacamite} = 0.491$), then for a thickness of 12 cm, the ratio of the two intensities is $I_{atacamite}/I_{bronze} = 1.29 \times 10^4$.

By studying the positive X-ray CTs of Fragment A, we detected some distinct, clearly shaped, strong dark formations, in different places and depths, signaling a much stronger X-ray absorption and therefore a different material than the atacamite material of the adjacent areas (e.g. gears). From Eq. (2) and setting $e^x = f$ (constant number), we get the result $I_a/I_b = f^{(\mu_b^* - \mu_a^*)}$ and because of $x > 0 \rightarrow f > 1$, so if

$$I_a/I_b > 1 \rightarrow \mu_b^* > \mu_a^* \quad (3)$$

The X-ray CTs present several imaging artifacts which were created by the hardware (instrument), software and by physical effects [20]. The main artifacts are the beam hardening (cupping effect due to the polychromatic energy emission of the X-ray tube source, see Fig. 3a), noise, scattering, streaking, shading and also ring and partial ring artifacts, from which most of them are also detected on the tomographies of the Mechanism.

Experimental

The dark shade formations on the X-ray positive CTs of the Mechanism

In positive AMRP CTs there are some formations with characteristic strong dark shades. These formations with well-defined shape and design are specific mechanical parts of the Mechanism. Two of them can be detected between the same axis gears *k1-k2* and *e5–e6* Fig. 3a. By using our functional Antikythera Mechanism models we observed that these two formations are spacers, preventing the cross engagement between gear teeth *e5–k2* (as we detected without the addition of these spacers in our models). This unwanted engagement immobilizes the rotation of the gears. [9]. According to the photometric profile of Fig. 3a, *k*-spacer is made of a different (corroded) material than the neighboring and on the same tomography, corroded gear material i.e. atacamite and also $\mu^*_{spacer} > \mu^*_{atacamite}$, see Eq. (3).

Another strong dark shade formation-spacer is detected between *c1–c2* gears and was placed by the ancient manufacturer in order to elevate gear *c1* to the same plane (height) as gear *b2*, since *c1* and *b2* are engaged Fig. 8b [1].

The ancient manufacturer had also placed five fixed, arc-shaped, supportive spacers on the Middle Plate, under the thin, large-diameter *b1* gear to enhance its stability. The three main (out of five) spacers are stabilized on the Middle Plate by pins Fig. 4. Regarding the two other additional spacers, the related *AMRP* CTs didn't show any stabilizing pins, but we detected some thin dark formations along the spacers' base and the Middle Plate. These dark formations which follow the pattern shape of the additional spacers are their soldering material on the Middle Plate Fig. 4 (insert) (see next chapter).

Small thickness formations with strong dark shades (soldering material) were also detected between the supporting base of the concrete gear *a1* and the Middle Plate Fig. 5c, d, middle contrast dark absorption formation between *d* spacer and the Middle Plate and also on the common spacer of *h1/i1* gears.

A large number of pins were detected on Fragment A. From the CTs it is visible that the ancient manufacturer stabilized the gears on their corresponding axes/shafts by

Table 1 Presents the relative solid metals and their most common chemical products by seawater corrosion (in relative large concentration), their corresponding mass absorption coefficient μ, their densities and linear absorption coefficient μ^* values, compared to atacamite values [29–42]

Probable element/compound of the dark/bright formations	μ (Mass coefficient $cm^2\ g^{-1}$) = μ^*/ρ @225 keV (NIST)	Density ρ ($g\ cm^{-3}$) [40, 41]	μ^* (Linear coefficient cm^{-1}) $\mu\ \rho$ (@225 keV)
Atacamite $Cu_2(OH)_3Cl$ (corroded copper/bronze) gears, shafts and plates	0.1328	3.7	0.491
Solid metals			
Cu (solid)	0.1394	8.9	1.240
Sn(β-white) (solid)	0.2604	7.3	1.900
Bronze (95%Cu + 5%Sn) (solid)	0.1455	8.8	1.280
Fe (solid)	0.1329	7.8	1.036
Pb (solid)	0.7577	11.3	8.562
Solder Pb (66%) + Sn (34%)	0.6443	9.9	6.378
Products of sea water corroded metals			
FeO (rust)	0.1230	5.7	0.701
Fe_2O_3 (rust)	0.1286	5.2	0.668
Fe_3O_4 (rust)	0.1290	5.0	0.645
FeOCl (rust)	0.1264	3.7	0.467
$Fe(OH)_2$ (rust)	0.1301	3.4	0.442
$Fe_2(OH)_3Cl$ (rust)	0.1286	1.8	0.231
FeO(OH) (rust)	0.1289	4.1	0.528
FeS_2	0.1278	4.9	0.626
SnO	0.2436	6.4	1.559
SnO_2	0.2303	6.9	1.589
$Sn_3O(OH)_2Cl_2$	0.2251	4.3	0.967
$PbCl_2$	0.5950	5.8	3.451
PbO	0.7119	9.5	6.763
Pb_2O_3	0.6913	8.3	5.737
$PbCO_3$	0.6142	6.5	3.992
Pb(OH)Cl	0.6292	6.2	3.901
PbS	0.6727	7.4	4.977
$PbSO_4$	0.5558	6.2	3.445
$Pb_3(OH)_2(CO_3)_2$	0.6311	6.1	3.849
Min. values for corroded solder $PbCl_2$(66%) + $Sn_3O(OH)_2Cl_2$ (34%)	> 0.3927	5.3	> 2.081
Summary			
Products of tin corrosion	$0.967 \leq \mu^* \leq 1.589$		
Products of lead corrosion	$3.451 \leq \mu^* \leq 6.763$		
Products of iron corrosion	$0.231 \leq \mu^* \leq 0.701$		

the use of pins Fig. 3b (and also used four pins for the stabilization of gear e4 on the gear e5) [9, 21]. According to the graph of Fig. 3b the material of the stabilizing pin, is much brighter than the adjacent *e1* gear, so it has a lower X-ray absorption than atacamite (*e1* gear) and therefore $\mu^*_{pin} < \mu^*_{atacamite}$ (see Table 1) (most of the pins appear in the CTs as brighter formations than the nearby gears).

Investigation of the X-ray dark shade unknown metal material

For the construction of the main parts of his creation (gears and plates) the ancient manufacturer used raw (binary) bronze sheet material [3]. After the spectrochemical analysis of the selected small sample, Price 1974 assumes that the small percentage presence of lead (0.3–0.6%) and iron (0.05%) could come from a soldering procedure and the existence of an iron pin respectively.

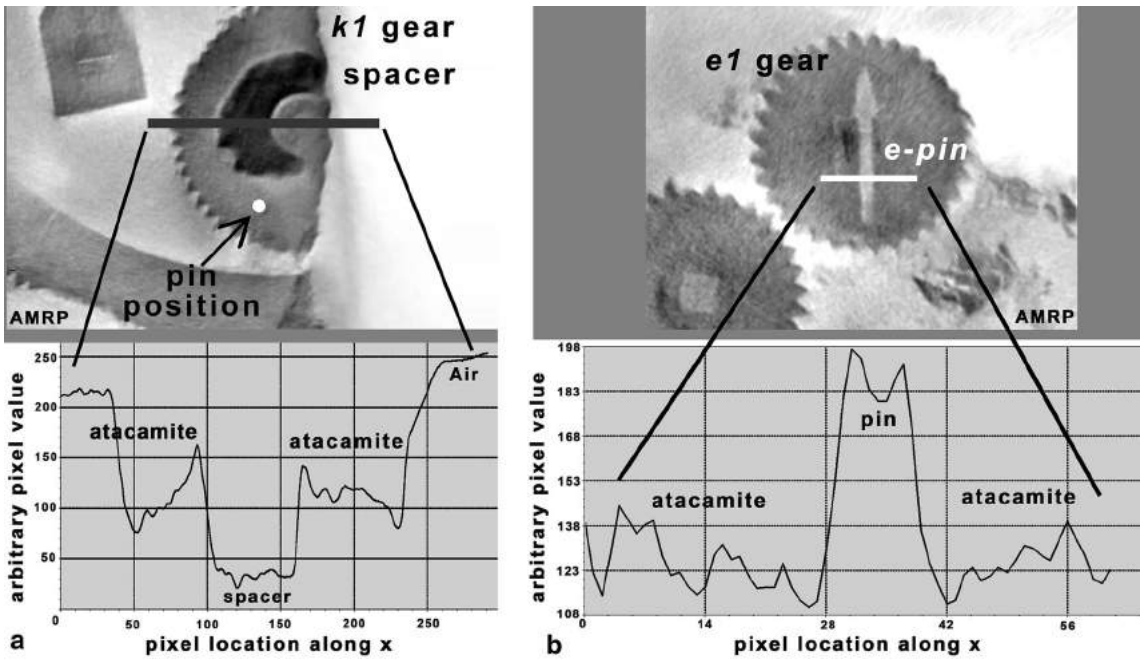

Fig. 3 **a** AMRP positive CT of *k1* gear. The graph shows the cut-through photometric profile (the area is marked with dark gray line). According to the graph the dark shade—X-ray absorption of the spacer, is much stronger than the neighboring gear material X-ray absorption (atacamite). The value variation of the gear grayscale is a result of inhomogeneities in the density/alloy composition-distribution/corrosion. The two strong peaks of the graph are due to cupping effect (beam hardening artifact) [20]. As it is clear, *k1*-spacer has been rotated from its original position about 36.3° CCW (the pin position of the pin&slot system, is marked with the white color dot). **b** Positive AMRP CT of gear *e1* and its well preserved, stabilizing pin. The cut-through photometric profile (the area is marked with white line), indicates that the unknown material of the pin has lower X-ray absorption than the neighboring area (gear) © AMRP

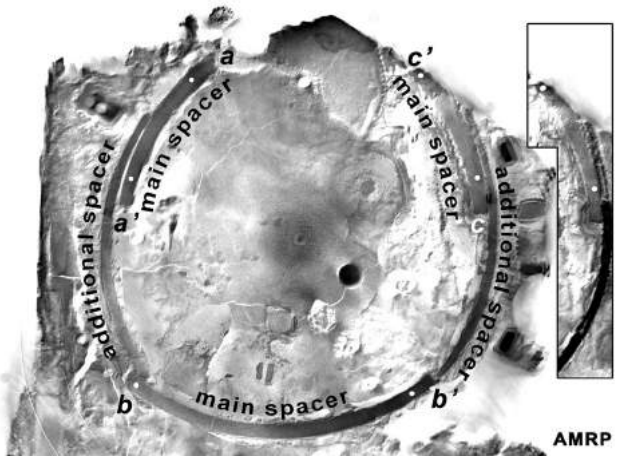

Fig. 4 **a** Multi-combined positive processed AMRP CT of the upper part of Fragment A shows the area behind the gear *b1* and the Middle Plate. The three main spacers *a*–*a*′, *b*–*b*′ and *c*–*c*′ with their stabilizing pins (white dots) and the two additional spacers are visible. Insert: the boundary between the two right spacers and the Middle Plate. The dark shade (arc) following the pattern shape of the additional spacer is the adhesive material. Note that there are not dark shades (adhesive material) between *c*–*c*′ main spacer and the Middle Plate © AMRP

Our analysis for the unknown metal material characterization was based on the different X-ray absorption of the materials, in relation to the corroded bronze absorption of the neighboring (same tomography) gears.

By studying the CTs it is evident that the photometric profile across a corroded bronze gear, displays small differences on the grayscale intensity Fig. 3. These differences were detected in random distribution, with limited dimensions and with unspecified shape. They have been probably created during the casting of the raw bronze material, as a lack of homogeneity of tin in the alloy or because tin (and also lead) tend to concentrate near the surface [21, 22]. Also the density of the bronze material after its total corrosion could have local area variations. These random differences do not affect our measurements. Even if the bronze alloy contained also a third metal e.g. lead in low percentage (about 1.5%), then the X-ray absorption would not change appreciably. The leaded bronze is not suitable for the metal sheet formation/production, because the metal becomes fragile after the process (hammering) or the working [3, 23].

From the graphs of Fig. 3 it is evident that the ancient manufacturer used another two different unknown metal/alloy materials with much different X-ray absorption than the absorption of the corroded bronze (gears). Of course these unknown metals/alloys during 2000 years under the

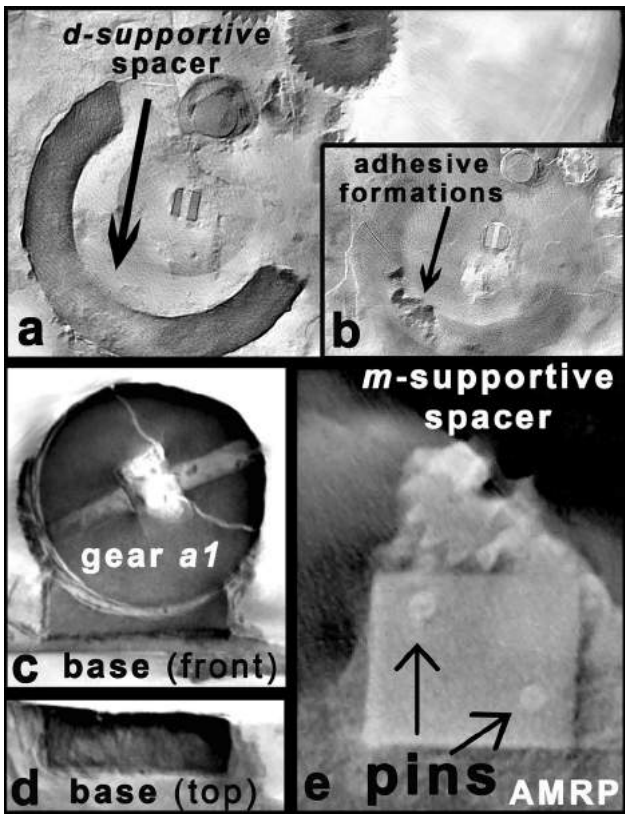

Fig. 5 **a** The positive AMRP CT shows the *C*-shaped *d*-supportive spacer of gear *d2*. **b** Positive CT between *d*-supportive spacer and the Middle Plate: the adhesive (solder) material of the *d*-spacer on the Middle Plate is visible. **c** The contrate gear *a1* and its *supportive* base (right side CT). **d** Top side view of the *a1*-supportive base close to the Middle Plate. The (small thickness) dark shades are the solder material of the *supportive* base on the Middle Plate. **e** The *m-supportive* spacer is stabilized on the Middle Plate by two pins ©AMRP

sea are also corroded/chemically changed by the reactions with sea water (as it happened with the bronze).

In order to characterize the unknown metal materials, we took into account the following parameters:

(1) we studied the common metals/alloys used during the era of 100BC (the probable era of the Mechanism construction),

(2) the constant μ^* of the candidate materials to be in agreement with their tomography imaging, i.e. darker formation materials have $\mu^* > \mu^*_{gear}$ and brighter formations $\mu^* < \mu^*_{gear}$,

(3) the most appropriate of the candidate metals for the corresponding position/operation on the Mechanism by real time testing the candidate metals in our models.

The most popular metals used in Hellenistic East Mediterranean and Greek metallurgy, technology and constructions, were iron, copper, tin, lead and their alloys, while zinc was not used widely [24–27]. From the shipwreck of the Antikythera, copper (bronze), tin, lead findings for various uses, were retracted (and also gold and silver which we excluded as candidate materials) [28].

By studying the related bibliography we refer to the most common corrosion products of the above mentioned metals by the seawater.

The corrosion products of lead in sea water could be $PbCl_2$, PbO, Pb_2O_3, $PbCO_3$, PbS, $PbSO_4$ and also $Pb(OH)Cl$ and $Pb_3(OH)_2(CO_3)_2$ [29–31].

The products of tin corrosion by the sea water are SnO, SnO_2 and $Sn_3O(OH)_2Cl_2$ [32–34].

The corrosion of iron by the sea water produces $Fe(OH)_2$, Fe_3O_4, FeO(OH), Fe_2O_3, FeOCl and also $Fe_2(OH)_3Cl$ [35, 36].

Using the X-COM calculating program for several chemical compounds, we calculated the mass absorption coefficient μ @ 225 keV of the possible metals/alloys as sea water corroded products, see Table 1 [37–42].

Correlating the Eq. (3) to the results of Table 1 and the graphs of Fig. 6, the unknown (corroded) metal of *k1*-spacer could be a corrosion product of Pb, Sn or corroded alloy of Pb–Cu (with much larger percentage of Pb), Pb–Sn–Cu (with much larger percentage of Pb and Sn-not as ternary bronze), Sn–Pb or Pb–Sn.

Initially, we assumed that the spacers of gears *e5–e6* and *k1–k2* were washers of solid lead, which is malleable and ductile. In our functional models, lead sheets in washer design shape, were placed as spacers on gears *e5* and *k1*. During operation of the two models and in a short time, these lead spacers were damaged by fragmentation and gradual partial detachment of the material into small pieces. Therefore, according to Table 1, we can assume that the ancient manufacturer used solid Sn or an alloy of Pb–Cu, Pb–Sn–Cu, Sn–Pb or Pb–Sn. However we consider unlikely the use of solid Sn (or in large percentage), because it was a very expensive metal at that time, costing 230 drachmas per talent (about 26 kg) in contrast to Cu costing 35 drachmas per talent [26]. Also unlikely is the use of an alloy of Pb–Cu because it is difficult to mix these two metals into a solid solution [43].

Pliny in *Natural History* (Book 34, Chap. 47) refers that there are two types of lead: the *black lead* (*plumbum nigrum*) i.e. the common lead and the *white lead* (*plumbum candidum*), i.e. tin [44]. He also refers that for the soldering process it is necessary to use an alloy consisting of two parts of *black lead* and one part of *white lead* (he refers to this alloy with the name *tertiarium*) and also with the help of an "oil", possibly colophonium or another type of resin [45, 46]. The alloy of Pb–Sn (and also Sn–Pb) with rosin-flux is used today as solder for the electronic parts on boards Fig. 7c, d [47, 48].

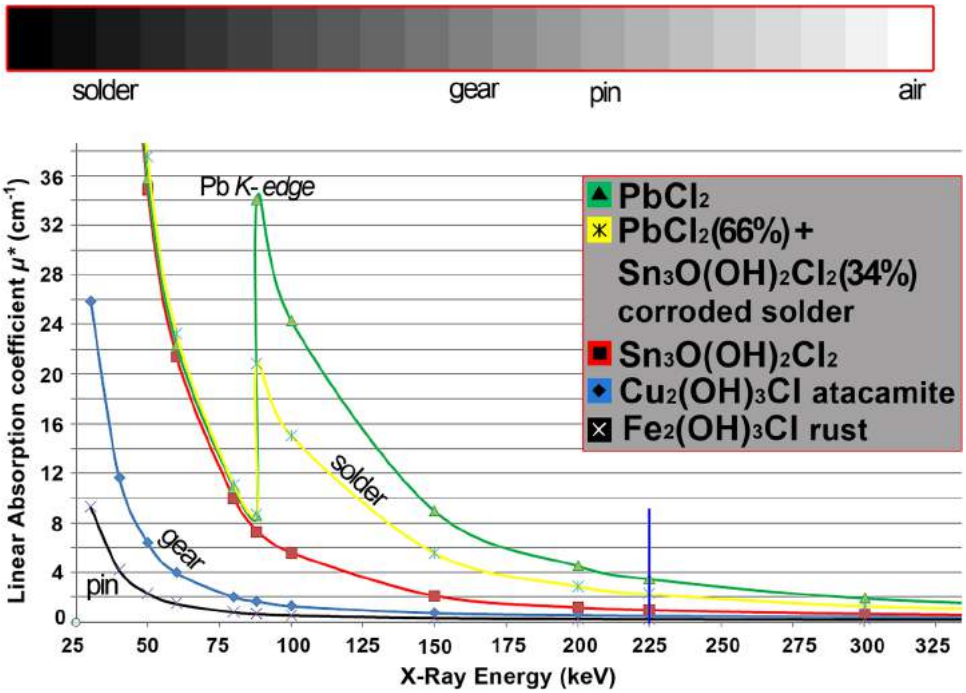

Fig. 6 Graphs of *linear absorption coefficient vs X-Ray energy* for the probable corroded metals of Fe, Sn and Pb relative to corroded bronze (atacamite). Processed data from XCOM, NIST [37]. Because of the existence of Pb on the corrosion product $PdCl_2$ and its presence on the corroded solder, the Pb K-absorption edge is also evident (@ 88 keV) on the corresponding curves (green and yellow color). The yellow color attenuation curve of *k1* corroded spacer/solder is located between the green (corroded Pb) and red color curves (corroded Sn). Its position depends on the percentage of the two corroded (metal) alloys: by increasing the percentage of corroded Pb on the solder material, the yellow curve approaches the green curve. After the energy of 90 keV the slope of the rust (pin) attenuation curve (black color) is close to zero and has the lowest μ^* of the materials. The corrosion products of Pb and Sn still have high absorption, because of high μ and also because of their density, which is high even after the metals corrosion, see Table 1. Presented on top is the gray shade photometric plate in 21 gradients. The corresponding shades of the material absorption, solder, gear and pin are also marked (data extracted from Fig. 3a, b). (Color figure online)

Another critical observation about the unknown metal characterization is the design/shape of the spacer between gears *k1–k2*, which seems that it has a *"C"* shape design and is not a circular perforated washer. Because of this design, the spacer needs to be stabilized on its corresponding position.

Pb–Sn alloys can be easily self-stabilized/soldered on copper or bronze material by direct heating Fig. 7c.

According to Fig. 3b the material of the *e*-pin (and also for most of the other pins) has a lower X-ray absorption than atacamite, ($\mu^*_{pin} < \mu^*_{atacamite}$). In Table 1, some of the chemical compounds of corroded iron (rust) could be possibly be the material of the corroded pins.

The Ω-retention bare and the supportive spacer constructions

The *d2* gear is placed just beneath gear *e3* Fig. 8a [1]. It is stabilized in its shaft between two pins and during its rotation is not in any contact with the Middle Plate. Its shaft is stabilized at only one point (i.e. on the Middle Plate), resulting to its strong nutation (the shaft, during its rotation cannot remain perpendicular on the Middle Plate) [9, 21, 50]. In order to eliminate the nutation of the *d*-shaft, the ancient manufacturer adapted a retention bar just above gear *d1*, logically in **Ω**-shape, which acted as a second bearing point of the *d*-shaft Fig. 8b. The Ω-shape bar was stabilized on the Middle Plate, but today only the base of this bar and the corresponding stabilizing pins are preserved in Fragment A. The same Ω-shape retention bar is also preserved on the interior mechanism of *Muhammad b. Abi Bakr* astrolabe (1221/2 AD), (see Price 1974, Fig. 43) [3, 51]. Also visible is the soldering (gray color) material with which the Ω-shape bar is stabilized on the astrolabe plate.

Finally it seems that even this design/construction was not good enough to completely eliminate the nutation of the system *d*-shaft/*d1*/*d2* gears, so the manufacturer was forced to adapt the *d-supportive* spacer. The *d-supportive* spacer with the characteristic *C-shape* design is located between the *d2* gear and the Middle Plate Fig. 5a and b [9, 21].

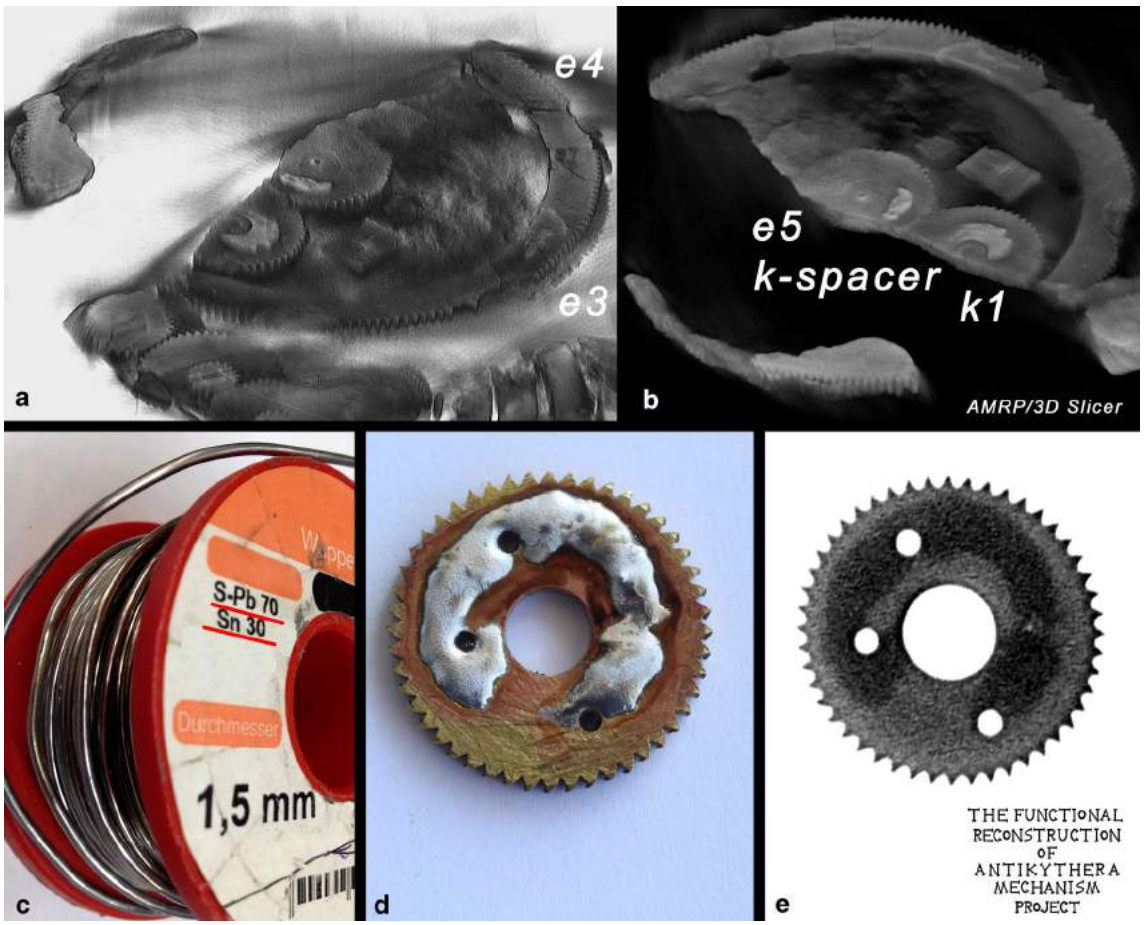

Fig. 7 **a** 3D reconstruction/visualization of gears *e3*, *e4*, *e5* and *k1*, based on the relative AMRP negative tomographies of Fragment A, with the use of *3D Slicer* software, processed by the authors [49]. **b** A different angle close up view of the 3D reconstruction in the area of *k1* gear and *k-spacer*. Note that just above the spacers there are the gears *k2* and *e6* [1]. **c** A typical electronics soldering wire with Pb 70% and Sn 30%. **d** Direct stabilization of Pb–Sn solder on a gear by heating. The color of the flux-rosin is also evident. **e** The corresponding X-ray radiography @120 keV of the gear on Fig. 6d

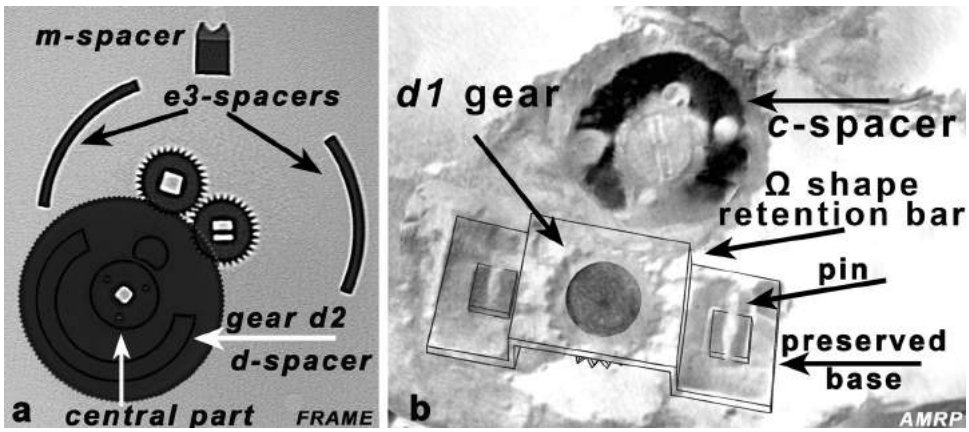

Fig. 8 **a** X-ray combined radiography @120 kV, of the FRAMe model gears *d2, b3, e1* and the twin spacers of *e3* gear and the *m*-spacer. Also visible are the *d*-spacer and the central circular part of gear *d2* stabilized on the main gear. **b** Processed (in 2D perspective) AMRP CT shows the *c*-shape dark shade spacer, which is fixed between gears *c1–c2*. Also detected are the two preserved bases of the *Ω* shape retention bar of *d1* gear ©*AMRP*. According to these bases, a computer graphics representation of the *Ω*-retention bar was sketched

The relative AMRP CTs didn't show any stabilization pins for the *d-supportive* spacer, but some small thickness, medium-contrast, dark formations were identified, which seems to be the soldering material of the spacer on the Middle Plate.

During the operation of our functional models, without the *d-supportive* spacer, we observed that the system *d2* gear, *d*-shaft, *d1* gear during its rotation was not stable, displaying a (minor) nutation, resulting to gear teeth conflicting/overlapping. By adding the *d-supportive* spacer, the system *d*-shaft/*d1*/*d2* gears, was stable and the problem was definitively solved.

It seems that another Ω-shape retention bar was adapted by the ancient manufacturer on gear *e3* in order to maintain gears *e5*–*e6* and *k1*–*k2* in their positions (see Wright's construction https://www.youtube.com/watch?v=eC54F4vv_8E at 09:08) [52]. Today only one base of this Ω-shape retention bar is preserved.

The two additional spacers just beneath the large gear *b1* were also stabilized on the Middle Plate by solder Fig. 4, because it seems that the three main spacers (stabilized by pins) were not enough to support the *b1* gear in a satisfying way.

Results and discussion

From the previous observations and analysis, it is clear that the ancient manufacturer used various metals/alloys of copper, tin lead and iron, for different parts of the Mechanism. Some spacers are stabilized on the Middle Plate by pins and some other spacers are, surprisingly, stabilized by solder.

It seems that after the assembly and during the first (?) use/operation of the Mechanism, some "mechanical problems" of the gears/shafts may have appeared—e.g. disengagement, displacement or nutation, (as was also observed in our functional models). So, in order to eliminate these problems, the manufacturer (or someone else) adapted some additional spacers to the Middle Plate (possibly not belonging to the initial design), by the use of solder. Of course, it was difficult or even impossible to stabilize the additional spacers on the Middle Plate by pins after the assembly of the Mechanism, because the pins were inserted in already existing holes. As a result he should either disassembly a large number of parts in order to drill holes for the pins or adapt additional spacers by soldering them. Of course after the disassembly and reassembly e.g. of a stabilizing pin, the stabilization could not be satisfactory (in contrast to the use of a screw as a stabilizer). Therefore the ancient manufacturer chose the procedure of soldering. Although solder has limited durability, the soldered additional parts are not under mechanical stresses and forces (compared to the gears and the shafts), thus offering a satisfactory stabilizing solution.

Undoubtedly, if the manufacturer had known these mechanical problems before the assembly of his construction, he would have stabilized the soldered (necessary) spacers by pins or he would have modified their initial design in order to avoid any "mechanical problems" and wouldn't have adapted additional-new parts after the assembly of his creation.

That's the reason why we believe that the existing specific design of the Antikythera Mechanism was the first of such a sophisticated design of the ancient manufacturer. Of course, such a complex machine, as is the Antikythera Mechanism, with so many particularities in its construction, presupposes the existence of numerous simpler or different design constructions [53].

The AMRP CTs "shed light" in different depths inside the Mechanism, giving the opportunity to solve lots of the mysteries and still helps researchers worldwide on the ongoing research about the Antikythera Mechanism. Of course the number of the unanswered questions which still arise by the study of the Mechanism, is high. The evolution of the technology on non-destructive material research, combined with the improved techniques in instrumentation and the imaging process, may give sometime in the future new information about this unique and remarkable machine of the Ancient world [54–56].

Acknowledgements We are very grateful to the AMRP for the license permission to study and use the CT images. Thanks are due to the National Archaeological Museum of Athens for the permission to capture and study the fragments of the Mechanism and the Deutsches Archäologisches Institut, Athens for the permission to use E. Seraf's photos. We would also like to thank prof. T. Economou of Fermi Institute-University of Chicago for his suggestions in X-ray CTs, the radiologist Mr. G. Giataganas and the radiology physician Mr. K. Kazlaris of Radiology Department of Papageorgiou General Hospital of Thessaloniki, Greece for X-ray radiography imaging of our models.

References

1. Freeth T, Bitsakis Y, Moussas X, Seiradakis JH, Tselikas A, Mangou H, Zafeiropoulou M, Hadland R, Bate D, Ramsey A et al (2006) Decoding the ancient Greek astronomical calculator known as the Antikythera Mechanism. Nature 444(7119):587–591
2. Edmunds MG, Freeth T (2011) Using computation to decode the first known computer. Computer 44(7):32–39
3. Price DS (1974) Gears from the Greeks: The Antikythera Mechanism, a calendar computer from ca. 80 B.C. Trans Am Philos Soc 64(7):1–70
4. Re A, Corsi J, Demmelbauer M, Martini M, Mila G, Ricci C (2015) X-ray tomography of a soil block: a useful tool for the restoration of archaeological finds. Herit Sci 3:4

5. Wright MT, Bromley AG, Magou H (1995) Simple X-ray tomography and the Antikythera Mechanism. PACT J Eur Study Gr Phys Chem Biol Math Tech Appl Archaeol 45:531–543
6. Allen M, Ambrisco W, Anastasiou M, Bate D, Bitsakis Y, Crawley A, Edmunds MG, Gelb D, Hadland R, Hockley P, Jones A, Mangou H, Malzbender T, Moussas X, Ramsey A, Seiradakis JS, Steele JM, Tselikas A, Zafeiropoulou M (2016) General preface to the publication of the inscriptions. The inscriptions of the Antikythera Mechanism. Almagest 7(1):5–35
7. Antikythera Mechanism Research Project (2018). http://www.antikythera-mechanism.gr. Accessed 12 Feb 2018
8. Ramsey A (2012) X-ray tomography of the Antikythera Mechanism. In: Proceedings of science, from Antikythera to the square kilometre array: lessons from the Ancients, Kerastari, Greece. http://www.atnf.csiro.au/people/atzioumi/Antikythera2012/presentations/X-ray_Tomography-Ramsey.pdf. Accessed 12 June 2018
9. Voulgaris A, Mouratidis C, Vossinakis A (2018) Conclusions from the functional reconstruction of the Antikythera Mechanism. J Hist Astron 49(2):216–238
10. Fernández-Montblanc T, Bethencourt M, Izquierdo A, González-Duarte MM (2014) Establishing the relationship between underwater cultural heritage deterioration and marine environmental factors. A comparative analysis in Bucentaure and Fougueux sites. In: Candelera R (ed) Science, technology and cultural heritage. Taylor & Francis Group, London
11. Ingo GM, De Caro T, Riccucci C, Angelini E, Grassini S, Balbi S, Bernardini P, Salvi D, Bousselmi L, Cilingiroglu A et al (2006) Large scale investigation of chemical composition, structure and corrosion mechanism of bronze archeological artefacts from mediterranean basin. Appl Phys A 83(4):513–520
12. Leyssens K, Adriaens A, Pantos E, Degrigny C (2004) Study of corrosion potential measurements as a means to monitor the storage and stabilisation processes of archaeological copper artefacts. In: Proceedings of metal 2004 National Museum (Canberra, Australia) ACT 2004, ABN 70 592 297 967
13. MacLeod ID (1981) Bronze disease: an electrochemical explanation. Inst Conserv Cult Mater Bull 7:16–26
14. Scott AD (1990) Bronze disease: a review of some chemical problems and the role of relative humidity. JAIC 29(2):193–206
15. Scott AD (2002) Copper and bronze in art, corrosion, colorants, conservation. Getty Publications, Los Angeles
16. Taylor RJ, MacLeod ID (1985) Corrosion of bronzes on shipwrecks: a comparison of corrosion rates deduced from shipwreck material and from electrochemical methods. Corr Nat Assoc Corr Eng 41:100–104
17. Voulgaris A, Mouratidis C, Vossinakis A (2018d) The green shades of the Antikythera Mechanism. J Coast Res (accepted)
18. Thomsen V, Schatzlein D, Mercuro D (2005) Attenuation of X-rays by matter. Spectroscopy 20(9):20–25. http://www.spectroscopyonline.com/tutorial-attenuation-X-raysmatter?id=&sk=&date=&pageID=1. Accessed 3 Apr 2018
19. X-ray Mass Attenuation Coefficients (2018) NIST. https://physics.nist.gov/PhysRefData/XrayMassCoef/chap2.html. Accessed 12 June 2018
20. Hsieh J (2015) Computed tomography: principles, design, artifacts, and recent advances. Spie Press, Bellingham
21. Wright MT (2006) The Antikythera Mechanism and the early history of the moon-phase display. Antiqu Horol 29(3):319–329
22. Hughes MJ, Cowell MR, Craddock PT (1976) Atomic absorption techniques in archaeology. Archaeometry 18(1):19–37
23. Deger-Jalkotzy S (2006) Ancient Greece. Edinburgh University Press, Edinburgh
24. Varoufakis G, Stathis EC (1971) Corrosion of ancient bronzes. Metallurgia 83(499):141–144
25. Orlandos A (1994) The structure materials of Ancient Greeks and the methods of their implementation. Archaeological Society of Athens (1955–56) and (1959–60), Athens
26. Varoufakis G (1996) Ancient Greece and quality. The history and checking of materials that marked the Greek culture. Aiolos Publications, Athens
27. Craddock PT (1978) The composition of the copper alloys used by the Greek, Etruscan and Roman civilizations. The origins and early use of brass. J Archaeol Sci 5:1–16
28. Kaltsas N, Vlachogianni E, Mpougia P (eds) (2012) The Antikythera Mechanism shipwreck: the ship, the treasures, the Mechanism, Exhibition Catalogue. National Archaeological Museum, Kapon Athens
29. Beccaria AM, Mor ED, Bruno G, Poggi G (1982) Corrosion of lead in sea water. J Br Corros Water 17:87–91
30. Pearson C (1987) Conservation of marine archaeological objects. Butterworth-Heinemann, London
31. Hamilton DL (1999) Methods of conserving archaeological material from underwater sites Conservation Research Laboratory Center for Maritime Archaeology and Conservation A&M University, Texas. http://nautarch.tamu.edu/CRL/conservationmanual/ConservationManual.pdf. Accessed 12 June 2018
32. Haixu L, Hao Y, Tao Z, Baoliang Y, Shaojiang Y, Yanling Z (2015) Effect of tin on the corrosion behavior of sea-water corrosion-resisting steel. Mater Des 84:1–9
33. Gao Y, Cheng C, Zhao J, Wang L, Li X (2012) Electrochemical corrosion of Sn 0.75Cu solder joints in NaCl solution. Trans Nonferr Met Soc China 22:977–982
34. Li D, Conway PP, Liu C (2008) Corrosion characterization of tin-lead and lead free solders in 3.5 wt% NaCl solution. Corros Sci 50(4):995–1004
35. Beccaria AM, Mor E, Poggi G (1983) Determination of the corrosion products of iron in sea water with and without sulphides. Werkst und Korros 34:78–83
36. Rémazeilles C, Neff D, Kergourlay F, Foy E, Conforto E, Guilminot E, Reguer S, Refait Ph, Dillmann Ph (2009) Mechanisms of long-term anaerobic corrosion of iron archaeological artefacts in seawater. Corros Sci 51:2932–2941
37. Database 8 (XGAM), Radiation Physics Division, NIST Standard Reference NIST, PML, Berger MJ, Hubbell JH, Seltzer SM, Chang J, Coursey JS, Sukumar R, Zucker DS, and Olsen K. https://www.nist.gov/pml/xcom-photon-cross-sections-database. Accessed 12 May 2018
38. Berger MJ, Hubbell JH (1987) XCOM: photon cross sections on a personal computer, NBSIR 87-3597
39. Hubbell JH, Seltzer SM (1996) Tables of X-ray mass attenuation coefficients and mass energy-absorption coefficients from 1 keV to 20 MeV for elements Z = 1 to 92 and 48 Additional Substances of Dosimetric Interest. Radiation Physics Division, PML, NIST
40. Mineral data—Hudson Institute of Mineralogy, open database of minerals, rocks, meteorites and the localities they come from. https://www.mindat.org/. Accessed 15 Jan 2018
41. Mineralogy Database. http://webmineral.com/data/. Accessed 12 Jun 2018
42. X-ray Mass Attenuation Coefficients (2018) NIST. https://physics.nist.gov/PhysRefData/XrayMassCoef/chap2.html. Accessed 4 Oct 2018
43. Jin-Chun K, Byung-Hyu K, In-Hyung M (1996) On some physical properties of nanostructured Cu–Pb alloy prepared by mechanical alloying. Nanostruct Mater 7(8):887–903
44. Pliny the Elder (1855) The Natural History. Taylor and Francis, Red Lion Court
45. Marabelli M (1991) In: Scott DA, Podany J, Considine BB (eds) Ancient & historic metals: conservation and scientific research

(the monument of Marcus Aurelius): proceedings of a symposium organized by the J. Paul Getty Museum and the Getty Conservation Institute, Marina del Rey, CA: Getty Conservation Institute
46. Beckmann J (1880) History of inventions, discoveries and origins. Bell & Sons, London
47. Life wire, types of solder. https://www.lifewire.com/types-of-solder-flux-818850. Accessed 10 June 2018
48. Life wire, types of solder flux. https://www.lifewire.com/types-of-solder-flux-818849. Accessed 10 June 2018
49. Fedorov A, Beichel R, Kalpathy-Cramer J, Finet J, Fillion-Robin J-C, Pujol S, Bauer C, Jennings D, Fennessy F, Sonka M, Buatti J, Aylward SR, Miller JV, Pieper S, Kikinis R (2012) 3D slicer as an image computing platform for the quantitative imaging network. Magn Reson Imaging 30(9):1323-1341. PMID: 22770690, https://www.slicer.org/. Accessed 29 Sept 2018
50. Wright MT (2011) The Antikythera Mechanism: reconstruction as a medium for research and publication. In: Staubermann K (ed) Reconstructions. Edinburgh University Press, Edinburgh
51. Field JV, Wright MT (1985) Early gearing. The Science Museum, London
52. Antikythera Mechanism demonstration, part 1 by Wright MT, https://www.youtube.com/watch?v=eC54F4vv_8E. Accessed 12 June 2018
53. Jones A (2017) A portable cosmos: revealing the Antikythera Mechanism, scientific wonder of the ancient world. Oxford University Press, New York
54. Lindstrom RM, Revay Z (2017) Prompt gamma neutron activation analysis (PGAA): recent developments and applications. J Radioanal Nucl Chem 314:843–858
55. Schillinger B, Calzada E, Lorenz K (2006) Modern neutron imaging: radiography, tomography, dynamic and phase contrast imaging with neutrons. Solid State Phenom 112:61–72
56. MacDonald BL, Vanderstelt J, O'Meara J, McNeill FE (2016) Non-destructive investigation of a time capsule using neutron radiography and X-ray fluorescence. Nucl Instrum Methods Phys Res Sect B Beam Interact Mater Atoms 367:46–52